PHYSICAL REVIEW D **92,** 073006 (2015)

Higgs-Strahlung: Merging the NLO Drell-Yan and loop-induced $0+1$ jet multiplicities

Dorival Gonçalves, Frank Krauss, Silvan Kuttimalai, and Philipp Maierhöfer

Institute for Particle Physics Phenomenology Physics Department, Durham University, Durham DH1 3LE, United Kingdom

(Received 14 September 2015; published 6 October 2015)

We analyze the production of a Higgs boson in association with a Z boson at hadron colliders in the Standard Model and some simple extensions. We show how multijet merging algorithms at leading and next-to-leading order for the loop-induced gluon fusion and the Drell-Yan-like quark-induced processes, respectively, improve the descriptions for various differential distributions, in particular those that involve the production of additional jets. The phenomenological studies focus on two relevant channels of Higgs boson decays, namely $H \to$ invisible and $H \to b\bar{b}$. We find sizable and phenomenologically relevant corrections to the transverse momentum and invariant mass distributions for the Higgs boson candidate. Thanks to the large destructive interference for the top Yukawa terms, this process is very sensitive to the magnitude and sign of a possible nonstandard top-Higgs coupling. We analyze the impact of this anomalous interaction on distributions and estimate constraints from LHC Run II.

DOI: 10.1103/PhysRevD.92.073006 PACS numbers: 14.80.Bn, 12.60.-i, 14.65.Ha

I. INTRODUCTION

The preeminent achievement of Run I of the LHC was the discovery of a scalar particle resonance [1], which so far proved largely consistent with the Standard Model (SM) Higgs boson [2,3]. This discovery not only marks the end of an era of searches for this elusive resonance, but it also heralds the beginning of a new era of exploration of the electroweak symmetry-breaking mechanism. The increased collision energy and luminosity of the LHC during Run II allows, in particular, precise measurements of the interactions of this new resonance with other known particles. At the same time, other new resonances interacting with the rest of the SM through the Higgs boson and new structures in the interactions of known particles will become a primary ground of renewed rigorous searches for physics beyond the Standard Model.

In this scenario, the associated production of a Higgs boson with a Z vector boson, $pp \to ZH$, also known as *Higgs-Strahlung*, is one of the most prominent paths toward an accurate understanding of the Higgs boson couplings. Remarkably, this production mode supplemented by jet substructure techniques can help to access the largest yet most challenging Higgs decay channel $H \to b\bar{b}$ [4], whereas the leading gluon-fusion and vector boson-fusion channels fail in this task due to overwhelmingly large QCD backgrounds. ATLAS and CMS already have reported first hints for this process [5,6]; while the former collaboration provided an upper limit on the event rate of 1.4 times the SM expectation, the latter observed an excess of events above the SM background with 2.1σ. Run II will thus clarify the situation concerning this process, fully establishing its existence and scrutinizing its dynamics. Ultimately, the ZH channel will shed light on the highly relevant branching ratio of Higgs bosons decaying into invisible final states, an important portal for interactions between the Standard Model and the dark matter sector. This channel provides one of the strongest constraints, where the current upper bounds at 95% C.L. reported by ATLAS and CMS are $\mathcal{BR}(H \to \text{inv}) < 0.75$ and 0.58 [7,8], respectively.

In the SM, ZH production is dominated by the Drell-Yan-like mode; see Fig. 1(a). At leading order (LO), it contributes to the total cross section at $\mathcal{O}(\alpha_{\text{EW}}^2)$. Another relevant production mode of ZH final states is gluon fusion, a loop-induced process mediated by quark loops, depicted in Figs. 1(b) and 1(c) and contributing at LO with $\mathcal{O}(\alpha_s^2\alpha_{\text{EW}}^2)$. These contributions have been discussed for example in Ref. [9].

At the level of the Feynman diagrams shown, these two subprocesses do not interfere, but it is important to stress that the latter, $gg \to ZH$, is part of the next-to-next-to-leading-order corrections to the total ZH production cross section. Here, we will treat the two process classes as separate categories, since this allows a more careful study of the respective QCD emission patterns. There are four major factors that guarantee that the gluon-fusion process is larger than the anticipated naive $\alpha_s^2 \approx 1\%$: i) it has a larger initial state color factor; ii) the process is driven by the large gluon parton distribution function; iii) the top Yukawa coupling y_t^{SM}, appearing in the box diagram in the place of one of the α_{EW} factors, is of order unity $y_t^{\text{SM}} \sim \mathcal{O}(1)$; and iv) the top-quark loop presents a threshold enhancement at $m_{ZH} \sim 2m_t$, which gives rise to relevant rates at the boosted regime $p_{TH} \sim m_t$.

On the phenomenological side, and in particular in the framework of Higgs boson coupling fits, the loop-induced

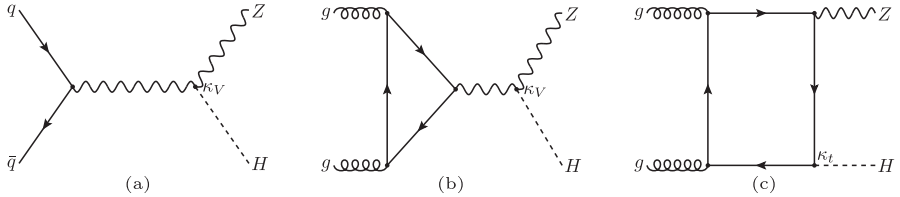

FIG. 1. Feynman diagrams for ZH production at leading order: (a) Drell-Yan-like; (b,c) gluon fusion.

contribution provides an additional probe to the size and the sign of the top-quark Yukawa coupling. In Figs. 1(b) and 1(c), the respective Higgs boson vertices lead to linear terms in κ_t and κ_V, where κ_t is a New Physics deviation to the top-quark Yukawa coupling and κ_V represents a potential rescaling of the HVV interaction vertices

$$y_t = \kappa_t y_t^{\mathrm{SM}}, \qquad g_{HVV} = \kappa_V g_{HVV}^{\mathrm{SM}}, \tag{1}$$

with $V = Z, W$. On the other hand, the WH and $qq \to ZH$ processes probe a single coupling strength, κ_W and κ_Z, respectively. At the LHC there are other known processes able to probe both their size and sign, e.g., Higgs boson production in association with a single top quark $pp \to tHj$ and the off-shell $H \to 4$ lepton production [3,10–18]. However, their experimental observation is challenging due to small rates and huge backgrounds.

In many analyses with complex final states, such as the ones emerging from the ZH processes discussed here, it has become customary to consider signals and backgrounds in bins of jet multiplicities; one of the most obvious examples being the process $H \to WW$, where the dominant $t\bar{t} \to WWb\bar{b}$ background can be fought with jet vetoes. Similarly, albeit less importantly, the same logic can also be applied to the $l^+l^-b\bar{b}$ final states typical for ZH production. There, jet vetoes can play a role similar to considering boosted topologies, which also suppress the $t\bar{t}$ and similar backgrounds. This motivates a more detailed study of jet-emission patterns in this process, where the tool of choice is the multijet merging technology that has already been used in a large number of Run I analyses, based on leading-order matrix element calculations.

In this work we study improvements arising from multijet merging techniques applied to the simulation of Higgs-Strahlung and the impact of the improvement which these techniques have experienced through the inclusion of next-to-leading order accurate matrix elements. The simulation comprises the following contributions:

(i) The Drell-Yan-like $pp \to HZ(ll) + 0, 1$ jets at next-to-leading -order (NLO) accuracy in QCD merged into a single inclusive sample. Representative Feynman diagrams are shown below, in Fig. 2.

(ii) The loop-induced gluon-fusion $pp \to HZ(ll) + 0, 1$ jets at leading order merged into a single inclusive sample. Cf. Fig. 3 below for a selection of contributing Feynman diagrams and our definition of the one-jet contribution in this channel.

Detailed predictions are presented for the invisible $Z(ll)H(\mathrm{inv})$ and hadronic $Z(ll)H(b\bar{b})$ Higgs boson decays. Using this framework, we also present a realistic phenomenological analysis deriving anticipated LHC Run II constraints to the (κ_t, κ_V) coupling parameters.

This paper is organized as follows. In Sec. II, we outline the basic structures of the Higgs-Strahlung process and point out the impact of higher jet multiplicities accounted for through multijet merging in a large variety of relevant distributions. In Sec. III, we use our toolkit to explore in detail possible new physics contributions. There, we derive

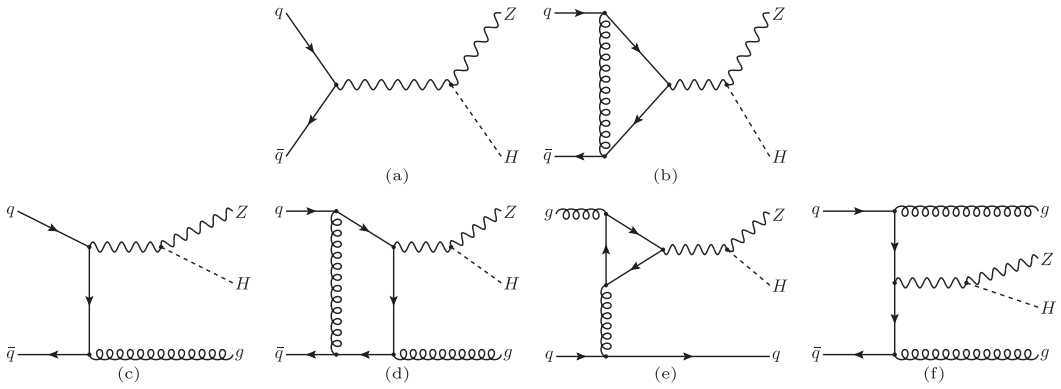

FIG. 2. Upper panel: representative Feynman diagrams for Drell-Yan ZH production at tree level (a) and at one-loop level (b). Lower panel: the same for ZHj at tree level (c), one-loop level (d,e), and corresponding real corrections (f).

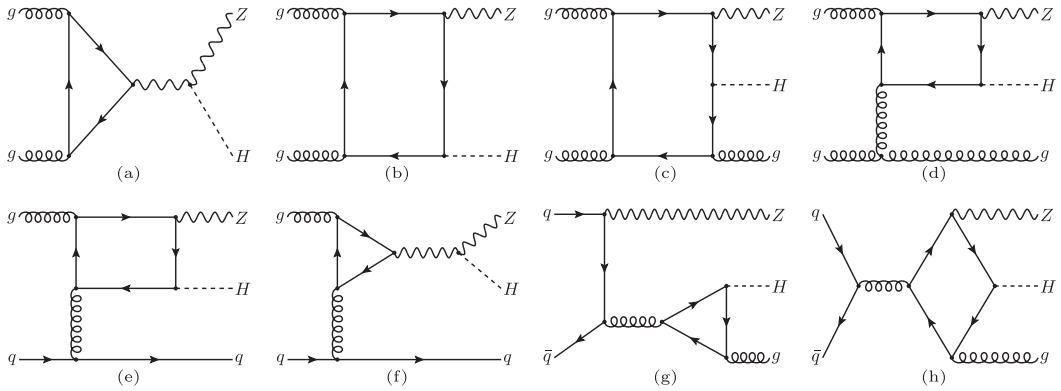

FIG. 3. Upper panel: representative Feynman diagrams for the loop^2 contribution. While the gluon-fusion contributions to ZH (a,b) and ZHj (c,d) are indisputably purely loop induced, the squared loop amplitude of diagrams with external quarks and a closed fermion loop (e–h) constitute a finite and gauge invariant subset of NNLO corrections to ZHj. The latter diagrams of course also interfere with the tree-level amplitude and are therefore included, on the amplitude level, in the NLO corrections as well [cf. Fig. 2(e)].

the LHC Run II constraints. We draw our conclusions in Sec. IV.

II. ZH PRODUCTION IN THE STANDARD MODEL

A. Higher-order corrections, multijet merging, and simulation setup

In this section we discuss in some detail the two dominant ZH production channels, namely the quark-induced Drell-Yan (DY) type Higgs-Strahlung and the loop-induced gluon fusion (GF), depicted at LO in Fig. 1. In particular, we study the impact of multijet merging to NLO accuracy for the DY and to LO accuracy for the GF contributions.

The DY component comprises the zero- and one-jet squared amplitudes at NLO, illustrated in Fig. 2's upper and lower panels, respectively. While the zero-jet GF part [Figs. 3(a) and 3(b)] is loop induced and therefore formally LO, in the context of multijet merging, it is more convenient to regard it as a subset of next-to-next-to-leading-order (NNLO) corrections in the sense of counting coupling constant powers with respect to the DY part. In our definition of GF with an extra jet, besides the loop-induced diagrams with three external gluons [Figs. 3(c) and (d)], we include all diagrams with a closed quark loop and an external quark line [Figs. 3(e) and 3(h)]. This definition, like the zero-jet gluon-fusion component, forms a finite and gauge invariant subset of NNLO corrections to ZHj and captures all diagrams which contain a squared Yukawa coupling at the squared amplitude level at NNLO QCD. Note that at the amplitude level there is an overlap of Feynman diagrams between DY and GF. For example, the diagram Fig. 2(e), when interfered with the tree-level amplitude, contributes to the NLO DY ZHj, while the same diagram Fig. 3(f) is also part of the GF amplitude, contributing at loop-squared NNLO.

Assuming that the invisible sector couples to the Higgs boson only, there is no interference between signal and background amplitudes in ZH, $H \to \text{inv}$. This is not true for $H \to b\bar{b}$ decays, in which case additional contributions must be considered. Besides the Higgs decay, $b\bar{b}$ pairs can be produced through QCD and through weak interactions, for example via $Z \to b\bar{b}$. Accordingly, when the $H \to b\bar{b}$ decay is treated as a part of the matrix elements as shown in Figs. 4(b) and 4(c), the amplitude interferes with the tree-level QCD continuum $l^+l^-b\bar{b}$ production Fig. 4(a). Analogously, the tree-loop interference with diagrams of the kind in Figs. 4(d)–4(g) occurs as a background. To capture spin correlations and off-shell effects in the gluon-fusion ZZ background, we take the loop-squared amplitude of diagrams like Figs. 4(f) and 4(g) into account with the full final state. At this point it is worth mentioning that due to spin considerations $Z \to b\bar{b}$ and $H \to b\bar{b}$ diagrams do not interfere. Some of these contributions have not been considered before in the literature.

While multijet merged predictions for the DY channel at NLO have been discussed in Ref. [19] and the merging in the loop-induced channel has been technically introduced in Ref, [20], here we are mostly interested in using this technology for detailed studies. In this context, it is worth pointing out that the theoretical precision for the DY channel at fixed order is known up to NNLO in the QCD and up to NLO in the electroweak perturbative series [21,22]. For the GF contribution, only estimates [23] of NLO corrections in the infinite top mass limit exist; this is due to the fact that a full calculation is hampered by the presence of many scales and, correspondingly, a prohibitive complexity in the necessary multiloop integrals. Similarly to the gluon-fusion process for Higgs boson and Higgs pair production, the approximation underlying the estimates mentioned above results in a large correction factor $K \sim 2$ to the overall cross section.

The SHERPA event generator [24] is used throughout this paper, supplemented with OPENLOOPS[25] for the calculation of all loop contributions and COLLIER[26] for the evaluation of tensor integrals. Finite width effects and spin

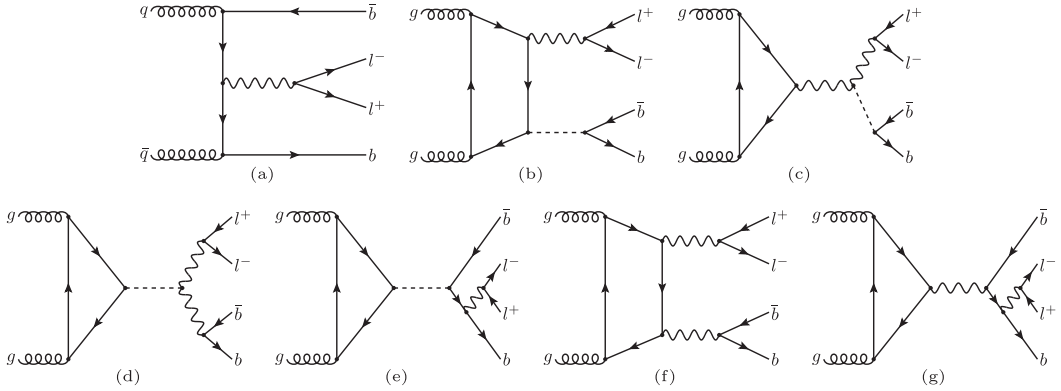

FIG. 4. Representative Feynman diagrams which contribute to the interference of the QCD continuum (a) with the signal (b,c) and background (d–h) when the Higgs decays into $b\bar{b}$, or when the $b\bar{b}$ pair is produced via a Z boson. The loop-induced ZZ_{GF} contribution (f,g) is furthermore included with full $l^+l^-b\bar{b}$ final state in order to capture spin correlations and off-shell effects.

correlations from the leptonic Z boson decay are fully accounted for in the simulation. For the multijet merging at leading order, we employ the ideas of Ref. [27], adapted for loop-induced processes in Ref. [28]. For the merging of next-to-leading order matrix elements, the MEPS@NLO algorithm [29] is used. This is implemented along the standard LO multijet merging algorithms in SHERPA, which also provides tree-level amplitudes, tools for infrared subtraction in the calculation of NLO QCD cross sections, and the simulation of parton showers, hadronization, hadron decays, etc. [30]. Throughout our studies we use the NNPDF3.0 parton distribution functions at NLO accuracy [31]. In our estimates of theoretical uncertainties, we focus on the usual renormalization and factorization scale variations by up to a factor of 2 in the fixed-order part of the simulation. From all these possible scale choices, we omit the ones in which the factorization and renormalization scale prefactors differ by a factor of 4. Since there is no higher-order calculation for the GF contribution, we not only consider the usual scale uncertainties, but we also consider the effect of higher orders on the total cross section (i.e., the GF rates account for $K = 2$). Since the K-factor estimate most likely is too naive an assumption, we estimate the associated uncertainty by varying the K-factor in the range from 1.0 to 4.0. We compare the resulting error bands with the ones obtained from the customary scale variations in Sec. II B. In addition, there are two more sources of uncertainties stemming from the combination of the fixed-order matrix elements with the parton shower. The first one is related to the jet cut used in the multijet merging, Q_{cut}, which we vary according to $Q_{\mathrm{cut}}/\mathrm{GeV} \in \{15, 20, 25\}$. In addition, the uncertainty related to the resummation performed numerically in the parton shower is estimated by varying the starting scales with factors in $\{\sqrt{0.5}, 1.0, \sqrt{2.0}\}$.

B. Invisible decays: $Z(ll)H(\mathrm{inv})$

Invisible Higgs decays occur in many models collectively referred to as "Higgs-portal" models; see, e.g., Ref. [32]. In these models, the Higgs boson is the mediator between the SM particles and an unknown sector with no other tangible interactions with the other Standard Model fields and therefore a prime candidate for dark matter. Higgs boson production in association with a Z is a particularly suitable channel for invisible Higgs decay searches due to its clean signature with large amounts of missing energy from the undetectable Higgs decay products recoiling against the (boosted) leptonic Z boson decays.

We start the study of the signal sample by applying some typical basic selection cuts. We require two same-flavor opposite charged leptons with transverse momentum $p_{Tl} > 20$ GeV in the pseudorapidity range $|\eta_l| < 2.5$ and an invariant mass in the region $|m_{ll} - m_Z| < 15$ GeV. Jets are reconstructed with the anti-k_T algorithm with resolution parameter $R = 0.4$ and $p_{Tj} > 30$ GeV in the pseudorapidity range $|y_j| < 5$, using FASTJET[33]. After applying these kinematic selections, the total signal cross section is strongly dominated by the DY component while the GF mode contributes with only $\mathcal{O}(10\%)$ to the total ZH cross section [9]. This finding seems to allow ignoring the GF channel for all practical purposes. However, selection cuts in searches for invisible Higgs decays typically include a minimum E_T^{miss} requirement, drastically reducing the overwhelmingly large $t\bar{t}+$ jets and $V+$ jets backgrounds. As shown in Fig. 5, applying such a cut substantially changes the relative composition of the signal cross section, and it enhances the relative contribution of the gluon-fusion production mode to up to $\mathcal{O}(30\%)$ of the DY mode. The origin of this increase can be mainly traced back to a harder transverse momentum spectrum triggered by a top quark threshold enhancement around $m_{ZH} \sim 2m_t$. This is supported by the finding in the left panel of Fig. 6, where we have varied the mass of the heavy quark running in the loop. In contrast, the DY contributions do not feature such an enhancement but rather show the typical s-channel suppression for large energies. Therefore, despite its small contribution to the inclusive cross section, the GF mode can

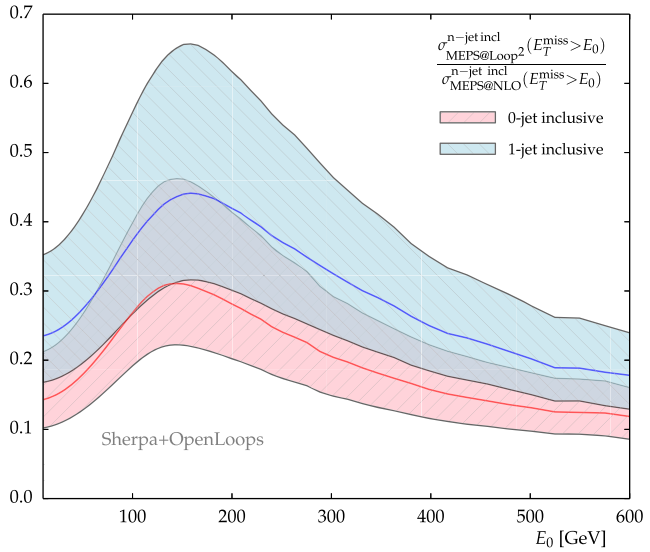

FIG. 5 (color online). Relative size of the gluon-fusion contribution to the cross section as a function of a minimum E_T^{miss} cut. We show individual curves for the total inclusive cross section and the one-jet inclusive cross section. Uncertainty bands are obtained from scale variations in the gluon-fusion sample, keeping the denominator fixed. The NLO Drell-Yan and the loop-induced gluon-fusion samples are both merged up to one jet, respectively denoted as MEPS@NLO and MEPS@LOOP^2.

become a significant player in the boosted regime, and a proper modelling of this component is of vital importance. In the right panel of Fig. 6, we show the theory uncertainties stemming from scale and K-factor variations, as detailed above, for the DY and the GF mode. Clearly, the K-factor variation leads to large effects, as the factor of 2 applied in both directions directly translates into an uncertainty, which is about twice as large as the effect of the standard scale variation in the GF mode. This size, about 30% or so, is typical for a merged sample at LO, especially in view of the fact that it is at least of order $\mathcal{O}(\alpha_S^2)$. In contrast, the scale uncertainty on the DY sample is much smaller, about 10%–20%.

In the lower panels of Fig. 6 (right panel), we also compare the missing transverse energy spectrum of the gluon-fusion component obtained from a simple LO matrix element plus parton shower simulation (LOOP^2+PS) with the one obtained from a merged calculation (MEPS@LOOP^2), taking into account matrix elements with up to one extra jet. In the boosted regime above $E_T^{\text{miss}} \geq m_t$, the LOOP^2+PS simulation significantly undershoots the spectrum of the one using merging technology, with the discrepancy reaching around 100% around $E_T^{\text{miss}} \sim 500$ GeV and further increasing with energy. This discrepancy has an origin similar to the finite top-mass effects in H + jets production studied in Ref. [11], namely that the extra jet emissions significantly impact the loop structure of the matrix elements. One can artificially suppress this effect by increasing the value of the top quark mass, thereby pushing the relevant scale for any loop structure effects to higher energies. This is shown in the left panel of Fig. 6, where the discrepancy between the LOOP^2+PS and MEPS@LOOP^2 simulations becomes much less severe.

Apparently, the effects induced by higher multiplicity jet-emission matrix elements are significant and beyond the scope of conventional parton showers alone. They can be

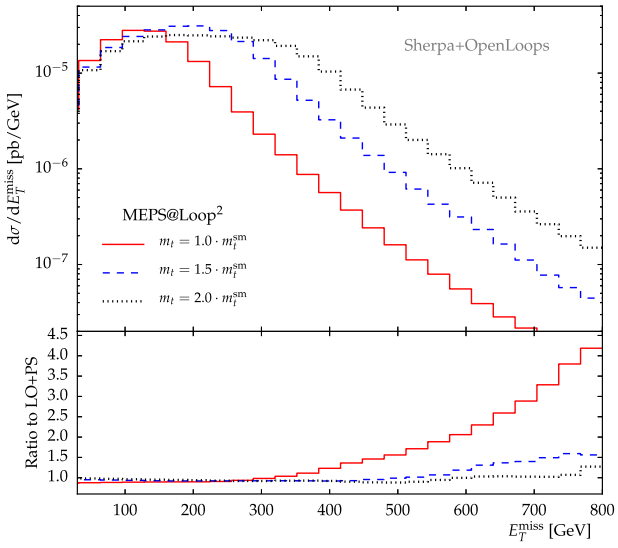

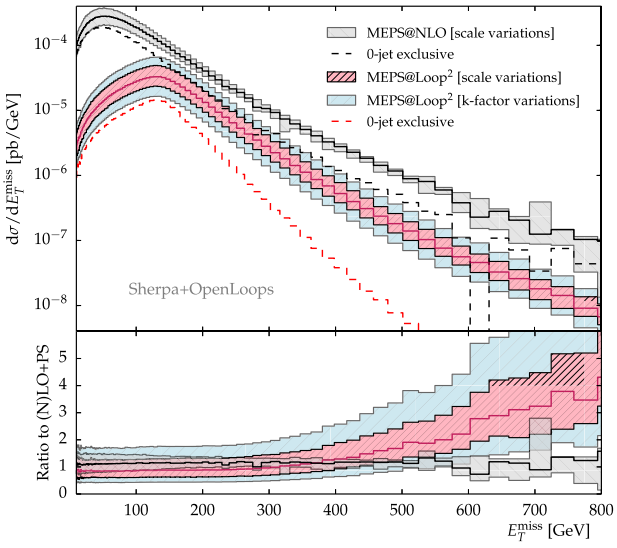

FIG. 6 (color online). Missing transverse energy distributions after basic selection cuts in the signal channel of the invisible Higgs decay search, assuming a branching fraction for $H \to$ inv of 1. Left panel: Varying the mass of the top-quark running in the loop in the GF contribution shows the threshold effect, extending to the tail of the distribution. Right panel: Uncertainty bands obtained from scale variations along with K-factor variations for the DY and GF contributions. The NLO Drell-Yan and the loop-induced gluon fusion are both merged up to one jet. The bottom panel presents the ratio between the MEPS@LOOP^2 to the LOOP^2+PS and the MEPS@NLO to the MC@NLO.

accounted for by applying matrix element merging techniques as demonstrated here, since they correctly fill those phase space regions that are typically problematic for the parton shower. This provides a very robust handle on theory uncertainties related to the application of vetoes in searches for invisibly decaying Higgs bosons in ZH production, which quite often are an important feature in the search strategies. Such vetoes on extra jet emissions are commonly used, cf., for example, Ref. [6], to suppress the backgrounds associated with Higgs-Strahlung, such as top-pair production. Following our discussion until now, we anticipate that a jet veto will further suppress the fraction of the loop-induced signal component, even when large $E_T^{\rm miss}$ is being required. A nice way to have some idea about the impact of a jet veto is to remind ourselves that the no-emission probability of an additional parton or jet with a transverse momentum $p_\perp$ off a quark q or a gluon g can be roughly estimated, to leading logarithmic precision, using Sudakov form factors. Schematically they are given by

$$\Delta_{q,g}(\mu_Q, p_\perp) = \exp\left[-C_{F,A}\int_{p_\perp^2}^{\mu_Q^2}\frac{\mathrm{d}q_\perp^2}{q_\perp^2}\frac{\alpha_S(q_\perp^2)}{\pi}\left(\log\frac{\mu_Q^2}{q^2}-\gamma_{q,g}\right)\right], \quad (2)$$

where $C_F = 4/3$ and $C_A = 3$ are the color charges of the quark and gluon and $\gamma_{q,g}$ are given by

$$\gamma_q = -\frac{3}{2} \quad \text{and} \quad \gamma_g = -\frac{\beta_0}{C_A} = -\frac{11}{6}+\frac{n_F}{9}, \quad (3)$$

with n_F the number of active flavors. The occurrence of the color factors easily motivates why the probability for not emitting a jet is larger for quark- than for gluon-induced processes.

Defining jet-veto efficiencies as

$$\epsilon(p_\perp^j) = \frac{\sigma_{0-\rm jet}^{\rm excl}(p_\perp^j)}{\sigma^{\rm incl}}, \quad (4)$$

that is the fraction of the inclusive cross section which survives a jet veto applied to jets above a certain transverse momentum cut $p_\perp^j$, we confront in Fig. 7 the simple Sudakov approximation for jet vetoes in the production of color singlet systems, i.e., ZH final states with an invariant mass of $m = m_H + m_Z$, with the exact results stemming from our more detailed simulation. It is remarkable in how far the simple approximation is able to reproduce the more exact result in the limit of small transverse momentum cuts applied in the jet veto. The results shown in the figure confirm that in the experimentally relevant ranges around 20 GeV, the gluon-fusion contribution is largely suppressed by jet vetoes due the initial state gluon's propensity to radiate.

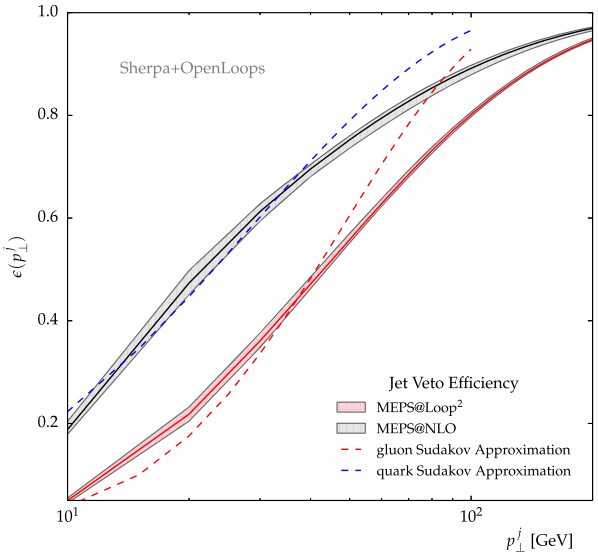

FIG. 7 (color online). Jet veto efficiencies for Drell-Yan-like contributions simulated via MEPS@NLO and for the gluon-fusion component calculated via MEPS@LOOP^2. We compare these predictions to simple Sudakov approximations.

A somewhat alternative way to suppress backgrounds is based on the observation that at large $E_T^{\rm miss}$ the Z and H bosons tend to be more or less back to back, rendering a selection cut on their relative azimuthal angle $\Delta\phi(ll, E_T^{\rm miss})$ an efficient means to improve the signal-to-background ratio. This is because additional jets would decorrelate the Z and the H in the transverse plane will effectively be vetoed by such a cut. As shown in Fig. 8, these assumptions hold for the Drell-Yan-like contributions. The distributions peak strongly at large azimuthal separations $\Delta\phi(ll, E_T^{\rm miss})$ and at small values of $|E_T^{\rm miss} - p_T^{ll}|/p_T^{ll}$. In the case of the gluon-fusion contribution, however, the enhancement of the distributions is much less pronounced in these regions, due to the larger level of QCD radiation decorrelating the ZH pair; configurations in which the Higgs recoils against a jet rather than the Z have a strong impact here. This is even the case at $|E_T^{\rm miss} - p_T^{ll}|/p_T^{ll} = 0$ and $\Delta\phi(ll, E_T^{\rm miss}) = 2\pi$. As can be seen in the lower panels of Fig. 8, even in this kinematic regime, there is a significant contribution from one-jet events in case of the gluon-fusion component, whereas this region is depleted of one-jet events for DY topologies. Performing a search binned in jet multiplicities, as it was done in Ref. [8], therefore retains sensitivity to the gluon-fusion component. In fact, as shown in Table I, the gluon-fusion component can be as large as 40% after applying typical selection cuts in the one-jet inclusive bin. Modelling this very contribution reliably requires the additional jet-emission matrix elements and makes the merging techniques applied here an indispensable tool.

Apparently, however, the gluon-fusion component was accounted for neither by ATLAS nor by CMS in their

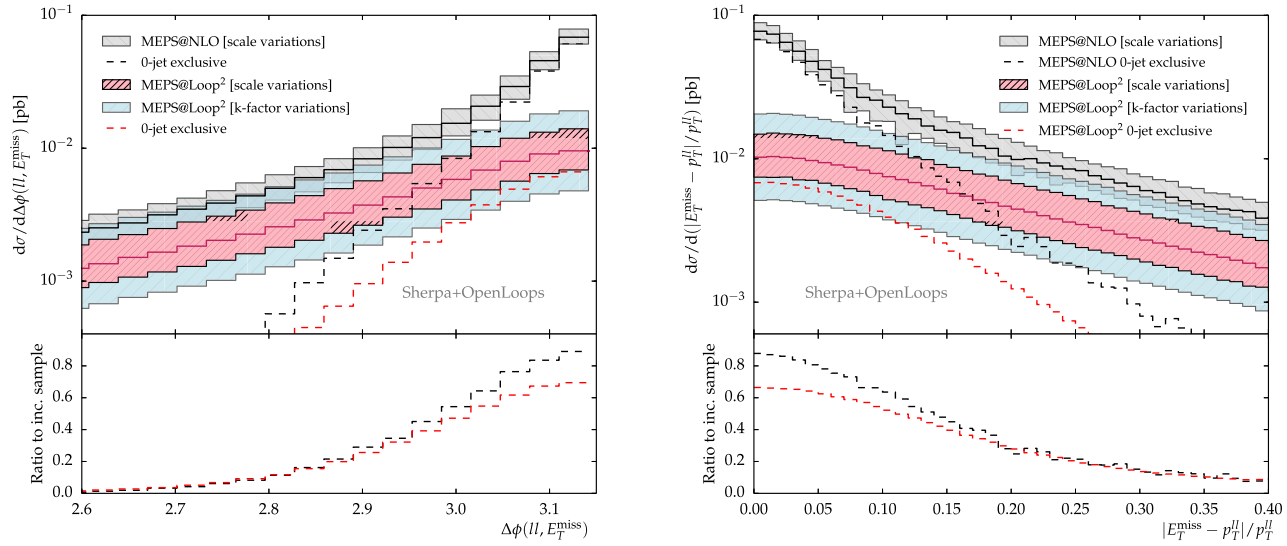

FIG. 8 (color online). Differential distributions for the major kinematic background suppression cuts in invisible Higgs decay searches.

searches for invisible Higgs boson decays at Run I [7,8]. We find that for the ATLAS analysis the jet-veto requirement in conjunction with selection cuts similar to the ones shown in Table I suppress the GF component to merely $\mathcal{O}(8\%)$ of the total signal rate. The CMS analysis, however, takes the one-jet exclusive bin into account separately, thereby retaining a larger sensitivity to the gluon-fusion component. We explicitly checked that the significance of the GF contributions in the one-jet exclusive bin at Run I energies is comparable to our findings in Table I.

C. Hadronic decays: $Z(ll)H(b\bar{b})$

We now analyze the Higgs-Strahlung channel for the $H \to b\bar{b}$ decay mode. In this case, the Higgs candidate is part of a multijet system that should contain not only its decay products but also the associated final state QCD radiation. This simple picture is blurred by initial state QCD radiation and additional particles originating from the underlying event "splashing" into the fat-jet system stemming from the Higgs boson decay. This complicated final state renders proper modelling of the QCD emissions an indispensable requirement for a successful and robust analysis of this process. In this section, we will therefore discuss, in particular, the relevance of multijet merging techniques.

To highlight the effect of higher-order effects and to quantify the impact of multijet merging, we follow the BDRS analysis [4] as a well understood benchmark: First, we impose some basic selection cuts requiring two same-flavor opposite charged leptons with transverse momentum $p_{Tl} > 30$ GeV, pseudorapidity $|\eta_l| < 2.5$, and invariant mass in the window 75 GeV $< m_{ll} <$ 105 GeV. We then impose the reconstructed Z boson to have a large transverse momentum $p_{T,ll} > 200$ GeV. In the BDRS algorithm, the hadronic final states of events are clustered into fat jets

TABLE I. Cut flow for typical selection cuts in invisible Higgs decay searches. We list the individual contributions from Drell-Yan production modes MEPS@NLO and the loop-induced MEPS@LOOP^2 component in $pp \to (H \to \text{inv})(Z \to e^+e^-, \mu^+\mu^-)$ at the LHC $\sqrt{s} = 13$ TeV. Uncertainties are obtained from scale variations as described in the text. For the loop-induced contributions, they become as large as the ones one would obtain from varying the K-factor in some cases. This is despite the fact that the K-factor variation error bands of the differential distributions in Figs. 6 and 8 exceed the scale variation error bands considerably.

	MEPS@NLO			MEPS@LOOP^2		
	σ_{incl} (fb)	$\sigma^{0-\text{jet}}_{\text{excl}}$ (fb)	$\sigma^{1-\text{jet}}_{\text{incl}}$ (fb)	σ^{incl} (fb)	$\sigma^{0-\text{jet}}_{\text{excl}}$ (fb)	$\sigma^{1-\text{jet}}_{\text{incl}}$ (fb)
$\lvert m_{ll} - m_Z\rvert < 15$ GeV, $p_{Tl} > 20$ GeV, $\lvert y_l\rvert < 2.5$	$34.5^{+9.1}_{-7.7}$	$21.1^{+5.3}_{-4.5}$	$13.4^{+4.1}_{-3.2}$	$4.9^{+2.4}_{-1.4}$	$1.74^{+0.8}_{-0.51}$	$3.2^{+1.6}_{-0.9}$
$E_T^{\text{miss}} > 120$ GeV	$9.7^{+1.8}_{-1.5}$	$4.98^{+0.88}_{-0.69}$	$4.74^{+0.95}_{-0.82}$	$2.9^{+1.4}_{-0.8}$	$0.95^{+0.45}_{-0.28}$	$1.96^{+0.97}_{-0.56}$
$\Delta\phi(ll, E_T^{\text{miss}}) > 2.5$	$8.0^{+1.5}_{-1.3}$	$4.97^{+0.88}_{-0.69}$	$3.04^{+0.61}_{-0.57}$	$2.4^{+1.2}_{-0.7}$	$0.95^{+0.45}_{-0.28}$	$1.42^{+0.74}_{-0.41}$
$\lvert p_T(ll) - E_T^{\text{miss}}\rvert / p_T(ll) < 0.25$	$6.5^{+1.2}_{-1}$	$4.81^{+0.83}_{-0.65}$	$1.65^{+0.33}_{-0.32}$	$1.57^{+0.78}_{-0.46}$	$0.88^{+0.41}_{-0.26}$	$0.70^{+0.37}_{-0.21}$

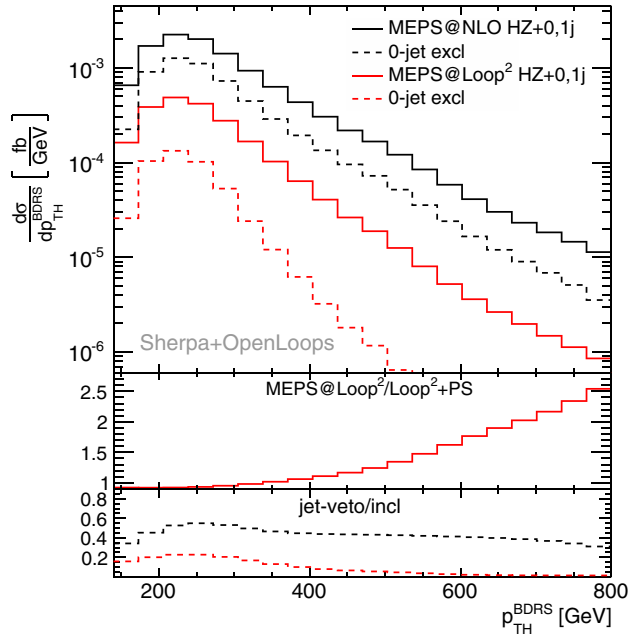

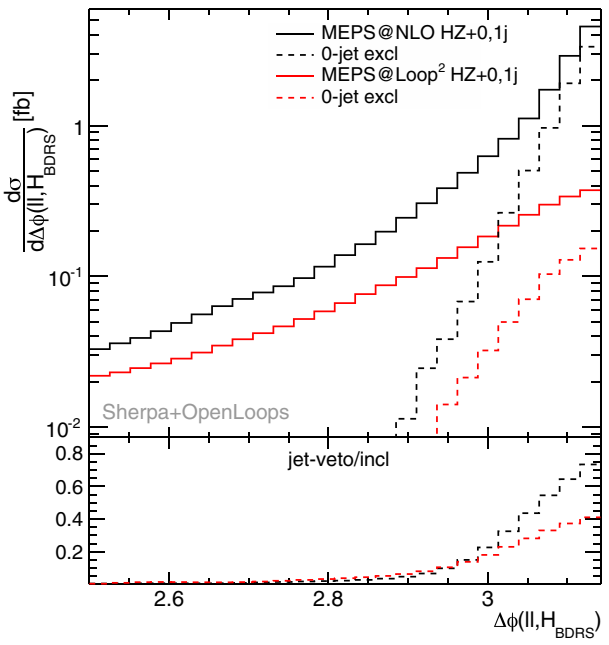

FIG. 9 (color online). Transverse momentum distribution of the filtered Higgs candidate p_{TH}^{BDRS} (left) and azimuthal angle $\Delta\phi(ll, H_{\mathrm{BDRS}})$ (right) between the Higgs boson and the Z candidate for $pp \to (H \to b\bar{b})(Z \to e^+e^-, \mu^+\mu^-)$ production at $\sqrt{s} = 13$ TeV. The NLO-merged Drell-Yan contribution is shown in black and the loop-induced LO-merged gluon-fusion mode in red. The bottom panel presents the ratio between the jet-vetoed and the inclusive sample, and the central panel (left only) presents the ratio between MEPS@LOOP^2 merged up to one jet and the parton shower sample.

using the Cambridge–Aachen algorithm with radius $R = 1.2$. The analysis demands at least one fat jet with $p_{TJ} > 200$ GeV and $|\eta_J| < 2.5$, acting as the candidate for the Higgs boson. This candidate is tagged through jet substructure techniques including the mass drop criteria and the requirement of three filtered subjets for which the two hardest ones need to be b tagged. Our analysis assumes a flat 70% b-tagging efficiency and a 1% mistag rate.

In Fig. 9 (left panel), we display the filtered Higgs jet transverse momentum p_{TH}^{BDRS}. In analogy to the E_T^{miss} in the case of invisible decays above, MEPS@LOOP^2 presents an enhancement with respect to the ZH LOOP^2+PS. This effect is noticeably smaller than in the invisible scenario; however, it is still relevant. In the invisible search, the requirement of $E_T^{\mathrm{miss}} > 120$ GeV leads to smaller invariant masses for the combined ZH system, which in turn sets the scale for the parton shower to populate the phase space with the emission of extra jets, while here the cut on the Z boson transverse momentum is at 200 GeV. The emission phase space offered to the parton shower thus is larger in the $H \to b\bar{b}$ case. As a consequence, in $H \to$ inv, the exact matrix elements, only included through the merging, have a larger impact. Additionally to this kinematic effect, the hadronic Higgs decay is naturally more sensitive toward QCD radiation which also induces some differences [34].

In Fig. 10 we present some of the QCD radiation dynamics in the invariant mass distribution for the filtered

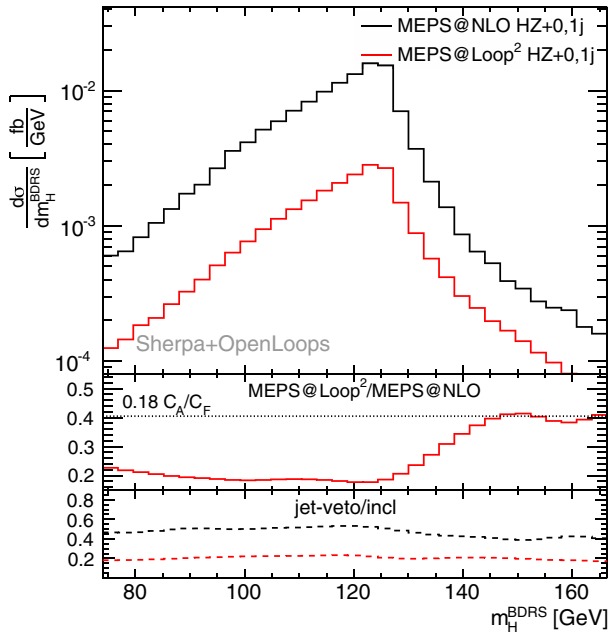

FIG. 10 (color online). Invariant mass distribution of the filtered Higgs fat jet candidate m_H^{BDRS} in $pp \to (H \to b\bar{b})(Z \to e^+e^-, \mu^+\mu^-)$ at $\sqrt{s} = 13$ TeV. The NLO DY contribution is shown in black and the loop-induced GF mode in red. Both samples are merged up to one jet. The central panel presents the ratio between the MEPS@LOOP^2 to the MEPS@NLO and the bottom panel the ratio between the jet veto to the inclusive samples.

Higgs. We first notice that the corrections to the production of the Higgs boson, that are performed here via the MEPS@NLO and MEPS@LOOP^2, contribute to the high mass tail $m_H^{\rm BDRS} \geq 125$ GeV. Extra parton emissions from the fixed order or from the parton shower arising from the ZH production can be reclustered in the Higgs fat jet, therefore enhancing its mass. On the other hand, the invariant mass region $m_H^{\rm BDRS} \leq 125$ GeV is populated from the shower radiation off the Higgs decays, therefore decreasing the reconstructed invariant mass $m_H^{\rm BDRS}$. Based on these observations, we can for instance understand the profile of the gluon-fusion contribution with respect to the Drell-Yan-like contribution shown in the bottom panel. While their effects at $m_H^{\rm BDRS} \leq 125$ GeV have the same source (i.e., shower emissions off the $b\bar{b}$ pair), at $m_H^{\rm BDRS} \geq 125$ GeV we observe a big enhancement that goes from $\mathcal{O}(18\%)$ to $\mathcal{O}(40\%)$ of the DY rate. This is a side effect of the larger radiation pattern arising from the gluon-fusion component, which benefits in particular from the larger initial state color charge $C_A/C_F = 9/4$. Indeed, that captures the size of the enhancement in a very good approximation $0.18 \times 9/4 \sim 0.4$. Besides, we notice that the jet veto suppresses the cross section by approximately a constant factor over the full $m_H^{\rm BDRS}$ distribution. This clearly indicates that both the parton shower off the Higgs decays and the corrections to the production are properly covering all the important phase space regions.

The $\Delta\phi(ll, H_{\rm BDRS})$ distribution shows that typical selection cuts of order $\Delta\phi(ll, H_{\rm BDRS}) > 2.5$ have a subleading impact on the inclusive rates for the signal component; see Fig. 9 (right panel). Additionally, in the presence of an extra jet veto, this azimuthal correlation requirement can be pushed even further, almost without extra losses. In Table II we display the impact of the cut $|m_H^{\rm BDRS} - m_H| < 10$ GeV and the extra-jet veto requirement. While the cut $\Delta\phi(ll, H_{\rm BDRS}) > 2.5$ has an imperceptible impact to both components, the extra-jet veto weakens the gluon-fusion signal contribution to a subleading level. Thus, if possible one should use other handles (than extra-jet vetoes) to the background suppression, especially for possible beyond the standard model (BSM) studies intrinsically associated to the loop-induced component. We will further comment on this in the following section.

TABLE II. Cross sections for the Drell-Yan and loop-induced components of $pp \to (H \to b\bar{b})(Z \to e^+e^-, \mu^+\mu^-)$ production at LHC $\sqrt{s} = 13$ TeV. Both samples are merged up to one jet, and the selection cuts follow the BDRS analysis that is described in the text. The rates are given in fb and account to 70% b-tagging efficiency. Hadronization and underlying event effects are accounted for.

	MEPS@NLO		MEPS@LOOP^2	
Cuts	$\sigma_{\rm incl}$	$\sigma_{0-\rm jet}$	$\sigma_{\rm incl}$	$\sigma_{0-\rm jet}$
BDRS reconstruction	0.37	0.18	0.07	0.02
$\lvert m_H^{\rm BDRS} - m_H\rvert < 10$ GeV	0.16	0.09	0.03	0.01

III. HIGGS-STRAHLUNG: BOOSTING COUPLING CONSTRAINTS

In this section we analyze the constraining power to the top-quark Yukawa coupling that can be derived from the $pp \to (H \to b\bar{b})(Z \to e^+e^-, \mu^+\mu^-)$ production. Following Eq. (1) we notice that the Drell-Yan component does not present any dependence on the top Yukawa κ_t but only on the size of the HVV coupling κ_V. On the other hand, the gluon fusion develops a dependence on both κ_V and κ_t.[1] Hence, we can write the matrix element for the ZH production as

$$\mathcal{M} = \kappa_t \mathcal{M}_t + \kappa_V \mathcal{M}_V, \tag{5}$$

where the t stands for the top Yukawa contributions and V for the contributions proportional to the HVV coefficient. The dependence on these coefficients can be straightforwardly translated to the Higgs p_{TH} spectrum via

$$\frac{d\sigma}{dp_{TH}} = \kappa_t^2 \frac{d\sigma_{tt}}{dp_{TH}} + \kappa_t\kappa_V \frac{d\sigma_{tV}}{dp_{TH}} + \kappa_V^2 \frac{d\sigma_{VV}}{dp_{TH}}. \tag{6}$$

Therefore, the p_{TH} distribution encodes the information about both the size and sign of the top Yukawa. To estimate the LHC sensitivity toward these coefficients, we consider the major backgrounds for Higgs-Strahlung, namely $t\bar{t} + \text{jets}$, $Zb\bar{b} + \text{jets}$, and $ZZ_{\rm EW}$. Besides these standard contributions, we also accounted for the loop-induced gluon-fusion $ZZ_{\rm GF}$ production depicted Fig. 4. The interferences with the QCD continuum as described in Sec. II A, see Fig. 4, were shown to be subleading in this analysis.

As for the signal, it is important to properly model the QCD radiation for the background components. The $t\bar{t}$ is generated with the zero-jet bin at NLO and merged up to three jets simulated at LO. The $Zb\bar{b}$ and $ZZ_{\rm EW}$ are generated via MC@NLO [35,36] and the loop-induced $ZZ_{\rm GF}$ at LO. The cut flow is presented in Table III. We avoid applying extra jet-veto requirements, since it would deplete the GF signal component as derived in the previous section. Notice that the loop-induced $ZZ_{\rm GF}$ production presents a non-negligible rate after the BDRS reconstruction; however, the Higgs mass window selection $|m_H^{\rm BDRS} - m_H| < 10$ GeV renders its contribution negligible.

In Fig. 11 we present the signal and background transverse momentum distributions after the selection cuts depicted in Table III. The background components are under control through the whole spectrum with the S/B ratio increasing toward higher energies. The negative top

[1]Only the relative sign between κ_V and κ_t is physical, and thus only positive κ_V is considered without loss of generality.

TABLE III. Cut flow for ZH + jets (gluon-fusion and Drell-Yan-like components), $t\bar{t}$ + jets, $Zb\bar{b}$ + jets, and ZZ + jets. Furthermore, we generate the EW and loop-induced QCD components. All simulations were performed with SHERPA+OPENLOOPS. The rates are given in fb and account to 70% b-tagging efficiency. Hadronisation and underlying event effects are taken into account.

Cuts	$ZH_{\rm GF}$ $\kappa_t=-1$	$ZH_{\rm GF}$	$ZH_{\rm DY}$	$t\bar{t}$ + jets	$Zb\bar{b}$ + jets	$ZZ_{\rm EW}$	$ZZ_{\rm GF}$
BDRS reconstruction	1.48	0.07	0.37	0.29	13.83	0.79	0.10
$\lvert m_H^{\rm BDRS}-m_H\rvert<10$ GeV	0.63	0.03	0.16	0.02	0.35	0.02	0.002

Yukawa $\kappa_t=-1$ displays an amount of events that surpasses the Drell-Yan and background components. It largely benefits from the σ_{tV} term that in the SM represents a destructive interference in the whole $p_{TH}^{\rm BDRS}$ distribution with a bigger magnitude than the other two terms σ_{tt} and σ_{VV} separately.

In Fig. 12 we show the projection of the reach in the ZH analysis for the coupling determination. We analyze the information from the different $p_{TH}^{\rm BDRS}$ bins via the CL_s method [37] and estimate the integrated luminosity necessary to exclude the negative top Yukawa solution at 95% C.L. A conservative systematic uncertainty of 50% is inferred to the GF channel. The BSM hypothesis can be excluded with ∼30 fb^{-1} of data.

IV. SUMMARY

We have studied the Higgs-Strahlung process at the LHC merging the zero and one-jet multiplicities for the Drell-Yan and loop-induced gluon fusion via the MEPS@NLO and MEPS@LOOP^2 algorithms, respectively. We have shown that the *multijet merging* is a fundamental ingredient to properly model the gluon-fusion component. The merging leads to significant contributions with respect to LO + PS simulations. For instance, for typical $H\to$ invisible searches at $p_{TH}\sim 500$ GeV, the correction factor is about 2.

A proper modelling of extra QCD emissions becomes even more important for the $H\to b\bar{b}$ decay, since the Higgs candidate is part of this multijet system. We scrutinized the signal contributions at the boosted kinematics and showed that MEPS@NLO and MEPS@LOOP^2 provide a good description for the relevant distributions. In particular, we observed significant improvements to the transverse momentum $p_{TH}^{\rm BDRS}$ and reconstructed mass $m_H^{\rm BDRS}$ for the Higgs candidate.

Higgs-Strahlung search strategies often rely on extra jet-veto requirements that, however, challenge the stability of perturbative expansions. We show that MEPS@NLO and MEPS@LOOP^2 considerably decrease the impact of jet vetoes on the uncertainties in comparison to MC@NLO and LOOP^2+PS, respectively. Furthermore, a larger suppression to the loop-induced component is observed. At the

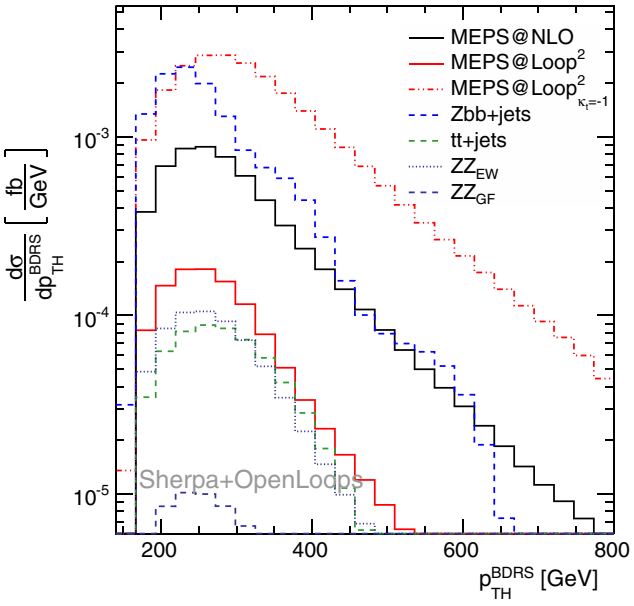

FIG. 11 (color online). Transverse momentum distribution of the filtered Higgs candidate $p_{TH}^{\rm BDRS}$ for the Higgs-Strahlung signal and backgrounds at $\sqrt{s}=13$ TeV. We also display the loop-induced gluon-fusion component for the BSM hypothesis with negative top Yukawa, $\kappa_t=-1$.

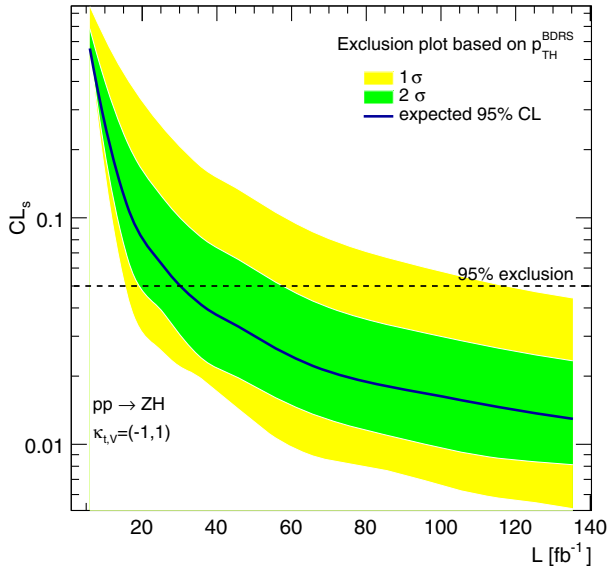

FIG. 12 (color online). Confidence level for disentangling the negative top Yukawa hypothesis $\kappa_t=-1$ from the Standard Model. We display the results for $pp\to(H\to b\bar{b})(Z\to e^+e^-,\mu^+\mu^-)$ based on the $p_{TH}^{\rm BDRS}$ distribution.

boosted regime, in particular, extra jet vetoes can deplete this signal component to subleading levels.

Finally, we also estimate the constraining power to the top Yukawa coupling via jet substructure techniques for $pp \to (H \to b\bar{b})(Z \to e^+e^-, \mu^+\mu^-)$ production. We perform a full analysis accounting for all the major background components that include, for instance, the electroweak and loop-induced QCD ZZ production. We conclude that the Higgs-Strahlung can be used to access both the size and sign of the top Yukawa coupling. Including conservative systematic uncertainties, the LHC Run II can exclude at 95% C.L. the negative top Yukawa solution $\kappa_t = -1$ with only ~ 30 fb^{-1}.

ACKNOWLEDGMENTS

F. K. and S. K. acknowledge financial support by the European Union Initial Training Networks MCnet (Grant No. PITN-GA-2012-315877). F. K. acknowledges additional support by HiggsTools (Grant No. PITN-GA-2012-316704) and by the ERC Advanced Grant MC@NNLO (Grant No. 340983).

[1] G. Aad *et al.* (ATLAS Collaboration), Phys. Lett. B **716**, 1 (2012); S. Chatrchyan *et al.* (CMS Collaboration), Phys. Lett. B **716**, 30 (2012).
[2] P. W. Higgs, Phys. Lett. **12**, 132 (1964); Phys. Rev. Lett. **13**, 508 (1964); Phys. Rev. **145**, 1156 (1966); F. Englert and R. Brout, Phys. Rev. Lett. **13**, 321 (1964); G. S. Guralnik, C. R. Hagen, and T. W. Kibble, Phys. Rev. Lett. **13**, 585 (1964).
[3] T. Corbett, O. J. P. Eboli, D. Goncalves, J. Gonzalez-Fraile, T. Plehn, and M. Rauch, J. High Energy Phys. 08 (2015) 156.
[4] J. M. Butterworth, A. R. Davison, M. Rubin, and G. P. Salam, Phys. Rev. Lett. **100**, 242001 (2008); T. Plehn, G. P. Salam, and M. Spannowsky, Phys. Rev. Lett. **104**, 111801 (2010); M. R. Buckley and D. Goncalves, arXiv: 1507.07926.
[5] S. Chatrchyan *et al.* (CMS Collaboration), Phys. Rev. D **89**, 012003 (2014).
[6] G. Aad *et al.* (ATLAS Collaboration), J. High Energy Phys. 01 (2015) 069.
[7] G. Aad *et al.* (ATLAS Collaboration), Phys. Rev. Lett. **112**, 201802 (2014).
[8] S. Chatrchyan *et al.* (CMS Collaboration), Eur. Phys. J. C **74**, 2980 (2014).
[9] L. Altenkamp, S. Dittmaier, R. V. Harlander, H. Rzehak, and T. J. E. Zirke, J. High Energy Phys. 02 (2013) 078; C. Englert, M. McCullough, and M. Spannowsky, Phys. Rev. D **89**, 013013 (2014); P. Agrawal and A. Shivaji, Phys. Lett. B **741**, 111 (2015).
[10] S. Biswas, E. Gabrielli, and B. Mele, J. High Energy Phys. 01 (2013) 088; S. Biswas, E. Gabrielli, F. Margaroli, and B. Mele, J. High Energy Phys. 07 (2013) 073; C. Englert and E. Re, Phys. Rev. D **89**, 073020 (2014).
[11] M. Buschmann, D. Goncalves, S. Kuttimalai, M. Schonherr, F. Krauss, and T. Plehn, J. High Energy Phys. 02 (2015) 038.
[12] N. Kauer and G. Passarino, J. High Energy Phys. 08 (2012) 116; F. Caola and K. Melnikov, Phys. Rev. D **88**, 054024 (2013); J. M. Campbell, R. K. Ellis, and C. Williams, J. High Energy Phys. 04 (2014) 060.
[13] A. Banfi, A. Martin, and V. Sanz, J. High Energy Phys. 08 (2014) 053.
[14] A. Azatov and A. Paul, J. High Energy Phys. 01 (2014) 014.
[15] C. Grojean, E. Salvioni, M. Schlaffer, and A. Weiler, J. High Energy Phys. 05 (2014) 022.
[16] E. Bagnaschi, G. Degrassi, P. Slavich, and A. Vicini, J. High Energy Phys. 02 (2012) 088.
[17] M. Schlaffer, M. Spannowsky, M. Takeuchi, A. Weiler, and C. Wymant, Eur. Phys. J. C **74**, 3120 (2014).
[18] M. Buschmann, C. Englert, D. Goncalves, T. Plehn, and M. Spannowsky, Phys. Rev. D **90**, 013010 (2014).
[19] G. Luisoni, P. Nason, C. Oleari, and F. Tramontano, J. High Energy Phys. 10 (2013) 083; S. Hoeche, F. Krauss, S. Pozzorini, M. Schoenherr, J. M. Thompson, and K. C. Zapp, Phys. Rev. D **89**, 093015 (2014).
[20] B. Hespel, F. Maltoni, and E. Vryonidou, J. High Energy Phys. 06 (2015) 065.
[21] O. Brein, A. Djouadi, and R. Harlander, Phys. Lett. B **579**, 149 (2004).
[22] M. L. Ciccolini, S. Dittmaier, and M. Kramer, Phys. Rev. D **68**, 073003 (2003); A. Denner, S. Dittmaier, S. Kallweit, and A. Muck, J. High Energy Phys. 03 (2012) 075; Comput. Phys. Commun. **195**, 161 (2015).
[23] L. Altenkamp, S. Dittmaier, R. V. Harlander, H. Rzehak, and T. J. E. Zirke, J. High Energy Phys. 02 (2013) 078.
[24] T. Gleisberg, S. Höche, F. Krauss, M. Schönherr, S. Schumann, F. Siegert, and J. Winter, J. High Energy Phys. 02 (2009) 007.
[25] F. Cascioli, P. Maierhöfer, and S. Pozzorini, Phys. Rev. Lett. **108**, 111601 (2012).
[26] A. Denner, S. Dittmaier, and L. Hofer, arXiv:1407.0087; A. Denner and S. Dittmaier, Nucl. Phys. **B844**, 199 (2011); **B658**, 175 (2003).
[27] S. Catani, F. Krauss, R. Kuhn, and B. R. Webber, J. High Energy Phys. 11 (2001) 063; F. Krauss, J. High Energy Phys. 08 (2002) 015; S. Hoeche, F. Krauss, S. Schumann, and F. Siegert, J. High Energy Phys. 05 (2009) 053.
[28] F. Cascioli, S. Höche, F. Krauss, P. Maierhöfer, S. Pozzorini, and F. Siegert, J. High Energy Phys. 01 (2014) 046.
[29] S. Höche, F. Krauss, M. Schönherr, and F. Siegert, J. High Energy Phys. 04 (2013) 027; T. Gehrmann, S. Höche, F. Krauss, M. Schönherr, and F. Siegert, J. High Energy Phys. 01 (2013) 144.

[30] F. Krauss, R. Kuhn, and G. Soff, J. High Energy Phys. 02 (2002) 044; T. Gleisberg and S. Hoeche, J. High Energy Phys. 12 (2008) 039; T. Gleisberg and F. Krauss, Eur. Phys. J. C **53**, 501 (2008); S. Schumann and F. Krauss, J. High Energy Phys. 03 (2008) 038; J. C. Winter, F. Krauss, and G. Soff, Eur. Phys. J. C **36**, 381 (2004); M. Schonherr and F. Krauss, J. High Energy Phys. 12 (2008) 018.

[31] R. D. Ball *et al.* (NNPDF Collaboration), J. High Energy Phys. 04 (2015) 040.

[32] A. Dedes, T. Figy, S. Hoche, F. Krauss, and T. E. J. Underwood, J. High Energy Phys. 11 (2008) 036; C. Englert, T. Plehn, D. Zerwas, and P. M. Zerwas, Phys. Lett. B **703**, 298 (2011); M. R. Buckley, D. Feld, and D. Goncalves, Phys. Rev. D **91**, 015017 (2015); P. Harris, V. V. Khoze, M. Spannowsky, and C. Williams, Phys. Rev. D **91**, 055009 (2015).

[33] M. Cacciari, G. P. Salam, and G. Soyez, J. High Energy Phys. 04 (2008) 063; Eur. Phys. J. C **72**, 1896 (2012).

[34] M. Dasgupta, A. Fregoso, S. Marzani, and G. P. Salam, J. High Energy Phys. 09 (2013) 029; M. Dasgupta, A. Powling, and A. Siodmok, J. High Energy Phys. 08 (2015) 079; A. Banfi and J. Cancino, Phys. Lett. B **718**, 499 (2012); G. Ferrera, M. Grazzini, and F. Tramontano, J. High Energy Phys. 04 (2014) 039; Phys. Lett. B **740**, 51 (2015).

[35] S. Frixione and B. R. Webber, J. High Energy Phys. 06 (2002) 029.

[36] S. Höche, F. Krauss, M. Schönherr, and F. Siegert, J. High Energy Phys. 09 (2012) 049; Phys. Rev. Lett. **110**, 052001 (2013).

[37] T. Junk, Nucl. Instrum. Methods Phys. Res., Sect. A **434**, 435 (1999).